Contents lists available at ScienceDirect

Advances in Water Resources

journal homepage: www.elsevier.com/locate/advwatres

Unlocking multimodal PET-MR synergies for geoscience

B. Brattekås [a],[*], J. Gauteplass [a], N. Brekke [b], M.A. Fernø [a], G. Ersland [a]

[a] Department of Physics and Technology, University of Bergen, Norway
[b] Center for Nuclear Medicine -PET, Department of Radiology, Haukeland University Hospital, Norway

A B S T R A C T

The recent combination of positron emission tomography (PET) and magnetic resonance (MR) imaging modalities in one clinical diagnostic tool represents a scientific advancement with high potential impact in geoscientific research; by enabling simultaneous and explicit quantification of up to three distinct fluids in the same porous system. Decoupled information from PET-MR imaging was used here, for the first time, to quantify spatial and temporal porous media fluid flow. Three-dimensional fluid distribution was quantified simultaneously and independently by each imaging modality, and fluid phases were correlated with high reproducibility between modalities and repetitive fluid injections.

1. Introduction

Diagnostic imaging is routinely used to map the interior of the human body, and recent advancements enable combined PET and MR imaging in a single, hybrid scanner to achieve new, complimentary insight. Much of the human body is soft porous membranes controlling vital liquid flow, where functional PET data corroborate anatomical MR data during simultaneous imaging. Although it may seem like a long leap, the gap between physiology and flow physics is short when it comes to imaging; and the same non-invasive methods are routinely used to characterize fluids and flow in porous sediments. Access to spatial and temporal flow in porous media by imaging is instrumental to determine the controlling parameters of carbon geo-sequestration, groundwater flow, aquifer remediation and hydrocarbon production.

Imaging techniques are typically divided into attenuation methods and explicit methods, where the former measures the gradual loss in photon flux intensity through the imaged sample and produces a time-averaged electron density distribution image (Heindel, 2011). Attenuation methods such as computed tomography (CT) imaging therefore rely on sufficient density differences of imaged phases (rock/fluid; bone/tissue) for high quality images. In contrast, explicit methods (e.g. MR and PET imaging), detect fluids in porous structures directly (Kulenkampff et al., 2008; Ersland et al., 2010a; Mitchell et al., 2013). MR imaging is rich in physics and a highly versatile tool that measures hydrogen in water or fat in our body, or as water, oil or gas in sediments. MRI is well suited for e.g. gas hydrate production studies (Ersland et al., 2010b) and wettability characterization (Howard, 1998). There are, however, some limitation to applicable rock types because certain minerals may decrease the MR image quality (Werth et al., 2010).

PET is primarily used in medical imaging, with occasionally reported geoscience use to visualize fluids in construction materials (Hoff et al., 1996), crystalline rocks (Degueldre et al., 1996), and sediments (Maguire et al., 1997; Khalili et al., 1998; Haugan 2000). Flow field imaging with PET in porous sandstones dates back to early 2000s (Ogilvie et al., 2001), and more recently in other geomaterials (Dechsiri et al., 2005; Kulenkampff et al., 2008, Boutchko et al., 2012; Pini et al., 2016). PET measures gamma radiation produced when a positron from a positron-emitting radionuclide annihilates with an electron, emitting a 511 keV gamma photon pair in opposite directions. A range of available positron-emitting tracers facilitate explicit tracking of different aqueous or gaseous phases, including CO_2 (Brattekås and Haugen, 2020; Fernø et al., 2015a). Quantitative assessment of core-scale fluid saturations with combined PET-CT was first reported by Fernø et al. (2015a). They found that saturation quantification was improved by PET compared to CT, attributed to the limited electron density contrast between fluid phases and an excellent PET signal-to-noise ratio. PET was also found to be superior for imaging CO_2 entry in low-porous materials; highly relevant for seal integrity during carbon geo-sequestration (Fernø et al., 2015b). Other examples of PET imaging in porous media include sub-core transport property characterization by parameter inversion (Vasco et al., 2018; Zahasky and Benson, 2018), capillary-dominated flow (Føyen et al., 2019), wormhole dynamics (Brattekås et al., 2017) and foam flow in fracture networks (Brattekås et al., 2019). A comprehensive description of PET systems and methods for earth science applications is detailed elsewhere (Zahasky et al., 2019).

Table 1

Overview of flow cycles. The arrows in the sequence name indicate increased (↑) or decreased (↓) source signal for each modality for each cycle. The PET source signal increased when injected water was labelled by F^{18}-FDG and decreased when non-labelled water was injected. The MR source signal increased by injection of H^+ atoms (H_2O-brine) and decreased when D_2O-brine displaced H_2O. During H_2O-brine-brine displacement, the MR source signal remained constant, denoted MR*const*.

Sequence	Brine injected	PET source signal (F^{18})	MR source signal (H^+)
Initial state	H_2O brine (static condition)	None	Full
Flow cycle PET↑-MR↓	D_2O brine w/ F^{18}-FDG	Increasing	Decreasing
Endpoint	D_2O brine w/FDG (static condition)	Full	None
Flow cycle PET↓-MR↑	H_2O brine	Decreasing	Increasing
Endpoint	H_2O brine (static condition)	None	Full
Flow cycle PET↑-MR*const*	H_2O brine w/FDG	Increasing	Full
Endpoint cycle	H_2O brine w/FDG (static condition)	Full	Full

Multimodal PET-MR quantify dynamic fluid saturations without the need for significant fluid density contrasts, and is therefore highly relevant in several porous media applications, although PET-CT scanners are more readily available. Porous media dispersion and adsorption is one example, crucial for ground water flow and miscible displacements in petroleum production, and of interest to engineers concerned with adsorbing agents like tracers, salts or surfactants. PET-MR imaging can potentially improve studies of carbon geo-sequestration by explicitly imaging the displacement of formation brine by CO_2-rich brine, enhancing the quantification of foam propagation, by determining the decoupled propagation of each foam component, or spatially determine wettability alterations of pores and seals during CO_2 injection.

Combined PET-MR imaging enables simultaneous quantification of up to three fluid phases in opaque systems, within the same field of view and time frame; unlocking a scientific advancement with potentially large impact in the geoscience community. The overall objective of this study was to evaluate multimodal PET-MR methodology for geoscientific research, and to demonstrate its capability of explicit, high-resolution imaging of displacement processes in sediments. This objective was achieved by directly comparing two- and three-dimensional PET and MR fluid signal maps during controlled miscible displacements, i.e. studying traced water flow where MR and PET signals were acquired from the injected aqueous phases using combinations of non-reactive radiotracer fluorodeoxyglucose, F^{18}-FDG, deuterium-water and water: The MR modality measures the density of H^+ atoms within the field of view, and the number of H^+ atoms in the pore space was controlled by injecting either D_2O-brine with no H^+ atoms or H_2O-brine with abundant H^+ atoms. The PET modality measures gamma radiation produced when a positron from a positron-emitting radionuclide annihilates with an electron, emitting a 511 keV gamma photon pair in opposite directions. To produce a signal detectable by PET, brine was labelled with radiotracer F^{18}-FDG. The validation of synergistic, multimodal multiphase quantification unlocks the potential usage for a wider range of geoscientific research areas.

2. Materials and methods

We studied three miscible flow cycles where PET and MR source signals were independently varied (Table 1). Spatial and temporal visualization of miscible fluid flow enable determination of local flow variations on the core and sub-core scales. A cylindrical Bentheimer sandstone sample (nominal length 100 mm; diameter 38 mm) coated in epoxy resin was fitted with Polyoxymethylene end-pieces and used for all injection tests. Nylon 1/8 in. Swagelok fittings and tubings were used to avoid magnetic disturbance in the proximity of the PET-MR instrument. The sandstone pore volume (28 cm^3) was fully saturated with brine (3.5 wt% NaCl in distilled H_2O) prior to the three miscible injection cycles. The core system was centrally mounted in a head coil of a Siemens AG® (Biograph mMR, Erlangen, Germany) whole-body, simultaneous PET-MR scanner. This PET-MR scanner operates each modal-

ity (PET and MR) independently, but in parallel, enabling simultaneous imaging within the same field of view without moving the core system between modalities.

For each injection cycle, two pore volumes (PV) of brine were injected with a constant volumetric flow rate (one cm^3/minute). Injected brine was labelled to produce a signal detectable by PET and/or MR using combinations of non-reactive radiotracer F^{18}-FDG, deuterium-water and water, detailed in Table 1. In flow cycle PET↑-MR↓ 367MBq of radiotracer was mixed in 200ml of D_2O-brine, and in Flow cycle PET↑-MR*const* 287MBq were mixed in 170ml H_2O-brine. Each flow cycle, with simultaneous imaging, lasted for one hour.

2.1. Imaging protocols

PET and MR imaging protocols must be separately optimized, to facilitate parameter determination for different time frames, and according to their respective strengths. We set imaging parameters to accommodate a high flow rate, reducing spatial voxel resolution to reduce acquisition time.

The MR image acquisition protocol was RAREst – *Rapid Acquisition with Relaxation Enhancement with short echo time* with echo time = 8.8 ms and rare factor = 4 was used. These settings produced 28 two-dimensional, coronal slices of 2 mm thickness within two minutes. The scanning time of two minutes covered the whole core volume and balanced adequate signal-to-noise ratio and temporal resolution required to capture dynamic behavior during injection cycles. Spatial and temporal MR resolutions are limited by the magnetic field and gradient strength (Werth et al., 2010).

The PET modality continuously records positron emission, and resolutions are determined during image post-processing. The temporal resolution was here set to two minutes to align with MR data, but could be significantly reduced to capture rapid flow processes. The spatial resolution of PET was 0.7x0.7x2mm, while MR resolution was set to 0.5x0.5x2mm in the x,y,z directions in this experiment. Section 3.2 The radiotracer F^{18}-FDG is a glucose analog commonly used in diagnostic imaging and was produced using an in-house cyclotron. Radionuclide half-life (109.7 minutes) was accounted for using embedded algorithms in the PET-MR software provided by the manufacturer. Unlike clinical PET-CT systems, PET-MR lack a direct way to obtain attenuation correction maps (Keereman et al., 2013) and the PET images were reconstructed without attenuation correction.

MR acquisition parameters can be optimized to yield explicit information about the rock structure (e.g. quantifying local pore size distributions by T2 mapping techniques), while PET acquisition parameters cannot. PET and MR signals at static conditions were, however, used to provide descriptive information of spatial fluid distribution on the centimeter scale. The number of disintegrations measured by PET and H^+ atom concentration measured by MR correspond to fluid volume by a linear correlation. In multiphase systems, local fluid saturations may be calculated based on this linearity (see e.g. Fernø et al., 2015a). At fully saturated conditions, this same relationship may be used to derive the
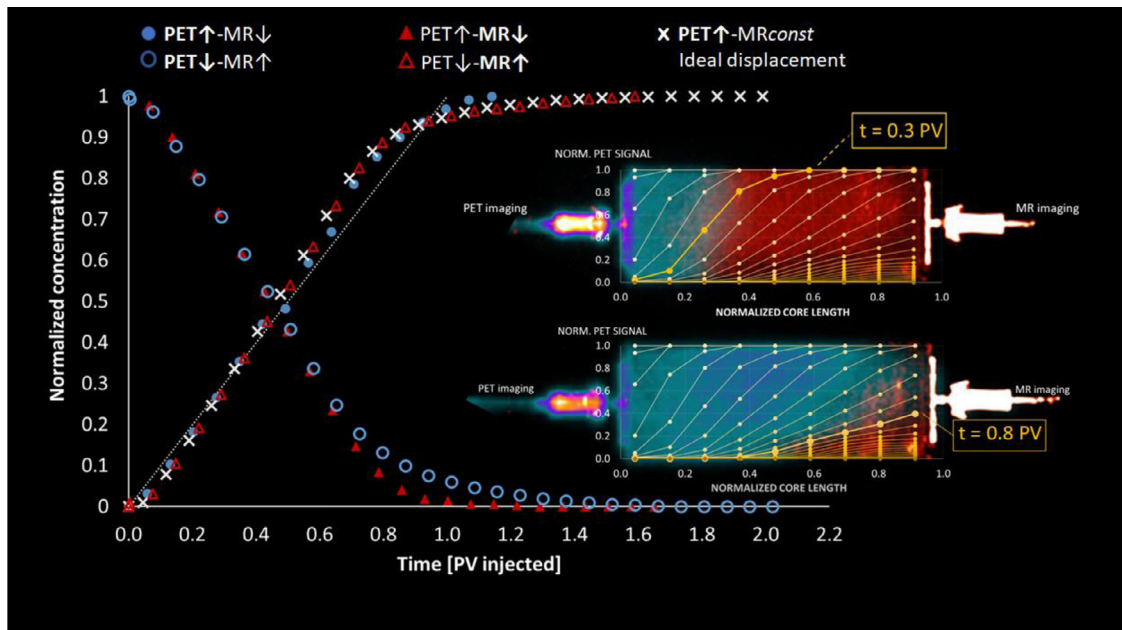
Fig. 1. Quantitative comparison of normalized source signal concentrations calculated from PET data (^{18}F-FDG concentration, blue circles) and MR data (H$^+$ concentration, red triangles) during miscible brine-brine displacements in a sandstone core plug (K = 821 mD; φ = 24.2%). Reproducibility was evaluated with three injection cycles (Table 1), and results confirm that both imaging modalities were able to accurately quantify changes in solute or H+ ion concentration over time with high accuracy. Signal half-life intersects at 0.5 PV, as expected. Insets show qualitative fluid front propagation (PET signal in blue and MR signal in red), overlain by quantitative PET signal profiles strength development at t = 0.3 PV and t = 0.8 PV. From t = 0.6 PV the displacement appears to deviate from ideal displacement (pore volume displaced equal to volume injected demonstrated by the white, dashed line), which was further investigated at the sub-core scale (Section 3.2).

local porosity values according to:

$$\phi_{x,y,z} = \frac{\left(\frac{signal}{voxel}\right)_{x,y,z}}{\left(\frac{signal}{voxel}\right)_{whole\ core}} \cdot \phi_{whole\ core},$$

where $\phi_{x,y,x}$ is the porosity at location $[x,y,z]$, and $\phi_{whole\ core}$ is the porosity of the whole core, calculated from weight measurements. Porosity was calculated in discretized flow elements, described in Section 3.2, i.e. the measured number of integrations per volume (signal/voxel) was averaged over several voxels to account for natural fluctuations in the PET instrument.

3. Fluid displacement

Miscible fluid displacement processes, combined with spatial and temporal information on fluid occupancy, enable quantitative analysis of rock heterogeneities that determine local variations in the overall flow pattern. Herein we demonstrate the potential of using decoupled, explicit fluid distribution information from PET-MR imaging to determine such variations at core (Fig. 1) and sub-core (Figs. 2 and 3) scales.

3.1. Core scale

An excellent agreement between fluid concentration calculated with decoupled PET and MR data was obtained between flow cycles – where labelled brine occupancy in the pore volume is equivalent to the normalized concentration of ^{18}F-FDG or H$^+$, respectively. Reproducibility was evaluated with three injection cycles (Table 1). Consistent core-scale concentrations for each cycle were calculated using decoupled MR and PET modalities, and results confirm that both imaging modalities were able to accurately quantify temporal concentrations with high accuracy. Cycle PET↑-MR↓ deviated slightly from the two subsequent cycles, due to slightly higher viscosity contrast (D$_2$O-brine approximately 20% more viscous and 10% denser than H$_2$O-brine). The small deviation was captured by both modalities: PET identified a slightly faster

displacement after 1 PV injected compared to the two other flow cycles: MR detected a decline between t = 0.7 - 1.2 PV, and the deviation was more pronounced compared to PET. This discrepancy arises as a result of the higher PET sensitivity and signal to noise ratio (SNR) compared to MR with the current settings.

SNR was directly derived for each imaging modality: for PET, the number of disintegrations measured per voxel within the core volume was divided by measured disintegrations per volume immediately outside of the core when the pore volume was fully saturated by F^{18}-FDG (at the end of cycle PET↑-MR↓), yielding SNR = 28:1. Similarly, for MR, the average signal per voxel within the core plug at maximum H$^+$ concentration (end of cycle PET↓-MR↑ and constant throughout the rest of the experiment) was divided by the core-adjacent noise level, providing SNR = 8:1. Hence, PET was able to detect lower signals compared with MR during cyclic flows. The difference between normalized concentrations measured by each modality was identified to be no more than 0.06 saturation points on the core scale.

Ideal displacement was observed for the first 0.6 PV injected, when the concentrations for each flow cycle deviated from unity between injected and produced volumes (Fig. 1), and appears to accelerate above ideal. The difference is, however, within the experimental uncertainty, resulting from the high injection rate and two-minute acquisition time: 0.07 pore volumes were injected during acquisition of each image, thus the fluid displacement front advanced and could not be accurately determined beyond 0.07 concentration points. The uncertainty was much lower at saturation end points, when the concentrations of F^{18}-FDG and/or H$^+$ were constant. The brine saturating the pore volume was fully displaced after t = 1.1 - 1.8 PV injected, corroborating previous miscible water displacements obtained by PET-CT imaging (Fernø et al., 2015a). A clear difference between PET and MR derived displacements was observed, where the H$^+$ concentration measured by MR appeared static from t =1.6 PV, while PET determined that maximum solute concentration was not reached until t = 1.77 PV. This difference is directly attributed to the excellent sensitivity and SNR of PET imaging, enabling small changes in concentration near the end-points to be distinguished.
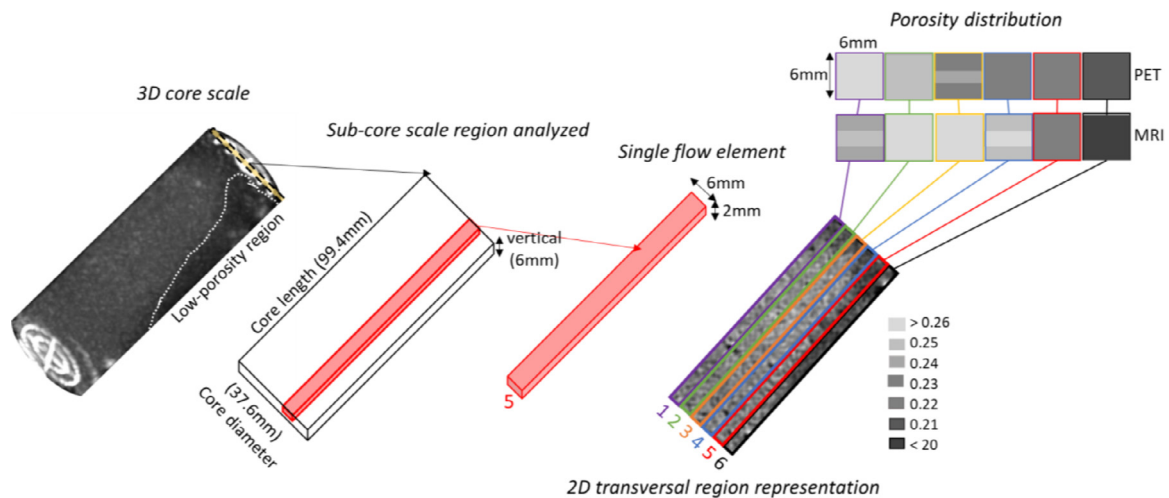
Fig. 2. Sub-core scale analysis was performed by quantifying flow in several smaller elements of the core. Core-scale images were transversally sliced and analyzed. Three slices of 2 mm thickness in the core middle represented overall core-scale behavior well and were chosen as the representative elementary volume for further analysis. The representative elementary volume was discretized into several flow elements, with cross-sectional areas of 6 x 2 mm^2. Porosity maps derived from the PET and MR signal intensities according to Eq. 1 are shown on the right.
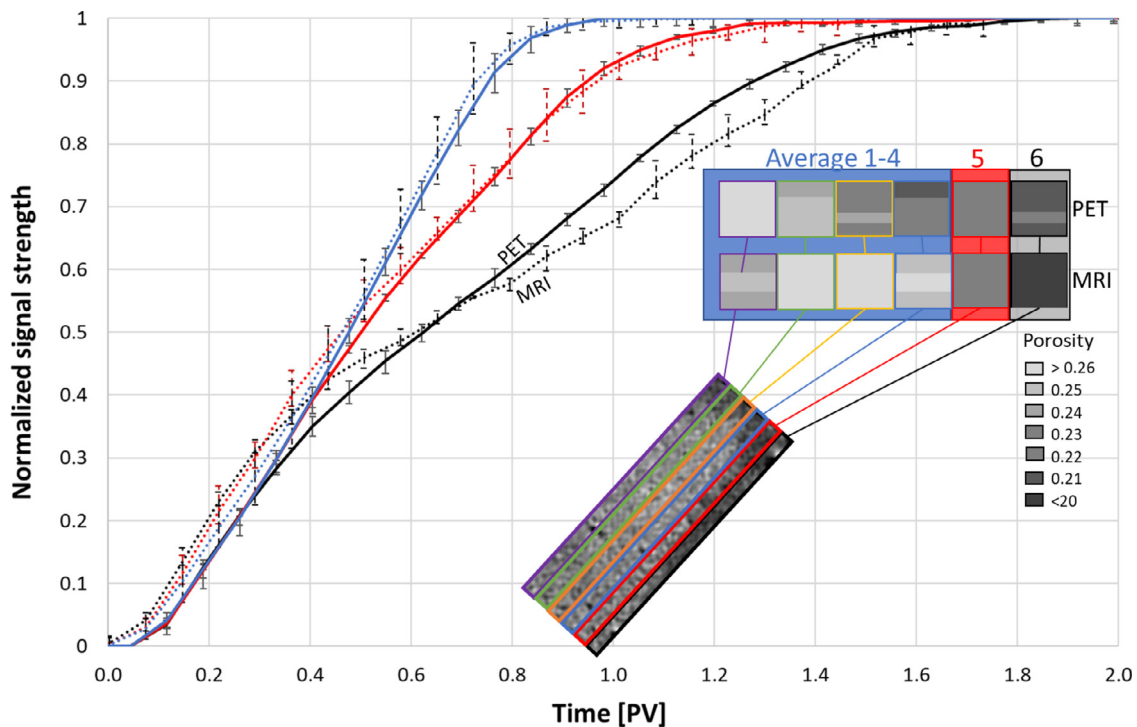

Fig. 3. Sub core-scale saturation development acquired using PET (solid-drawn lines) and MR (dotted lines) imaging. The graph colors correspond to the flow elements: the 1 — 4 average is shown in blue, while sub-core scale elements 5 and 6, where the low porosity heterogeneity influence flow, are shown red and black, respectively. The saturation development in flow elements 5 and 6 was significantly slower than the 1-4 average, and responsible for core scale deviation from ideal displacement. All signal intensities were normalized to the maximum intensity of each flow tube. The figure shows signal increase cycles PET↓-MR↑ (MR signal) and PET↑-MRconst (PET signal), which overlapped on the core scale.

The concentration development after t = 1.1 PV, needed sub-core analysis to to describe the slower-than-expected increase.

3.2. Sub-core scale

Dynamic fluid distribution images were digitally sub-divided to determine local displacement variations. The core was first sliced transversally, and each slice was divided into smaller flow elements parallel to the general flow direction (Fig. 2), similar to the discretization approach used by Pini et al. (2016) and Zahasky and Benson (2018). This enabled quantification of spatial structural variation which in turn dictates local flow capacity (Krevor et al., 2011). Three transversal slices

in the core middle captured the overall flow behavior and were used in the sub-core analysis as representative elementary volume. Each of the three slices hold six flow elements spanning the entire core length; and structural differences in the core could be spatially quantified to determine the cause for displacement heterogeneities. Sub core-scale porosity could be calculated for each flow element using information from both PET and MR (Fig. 2), and demonstrated that a region with lower porosity, not known *a priori*, existed within the pore space. This region was visually observed in the initial MR scan when the core was filled with H_2O-brine. The porosity within the pore space was determined to range between 18 and 26% by MR (variation of 8%) and between 23

and 28% by PET (5% variation). The smaller variation measured by PET reveals that attenuation of photons in areas of higher density (i.e. lower porosity) was not significant for the small core system at the radiation level used in out experiment, hence attenuation correction was not necessary.

The cause for non-uniform miscible displacement was identified to be the low-porous heterogeneity (Fig. 3). Low-end porosity values were predominant in flow elements 5 and 6, while flow elements 1-4 (Figs. 2 and 3) did not exhibit significant porosity heterogeneity. Signal intensities therefore increased or decreased swiftly in flow elements 1-4, while a slower saturation development was observed in the flow elements incorporating the heterogeneity (Fig. 3). Flow deviation in low-porosity flow elements was well captured by both PET and MR, with good agreement between the modalities in flow elements 1 through 5 (Fig. 3). Sub-core flow element 6 was determined by both PET and MR to have lower porosity (Figs. 2 and 3) and exhibited the slowest saturation development. The slow core-scale displacement near end-points was largely caused by flow element 6, including the differences in displacement end-point, measured at 1.6 PV by MR compared to 1.77 PV by PET. The excellent sensitivity and SNR achieved by PET imaging contributes to a lower uncertainty interval compared to MR (Fig. 3), and the slow, continued development in fluid concentration within flow element 6 was visible for longer. MR imaging could not distinguish dynamic concentration changes after 1.6 PV injected, because the relative signal change within the flow element was low compared to the high adjacent noise level. Thus, discrepancies between results acquired by PET and MR imaging in this study were amplified by the differences in SNR.

The findings from this integrated imaging study (presented in Sections 3.1 and 3.2) demonstrated that small-scale heterogeneities in a presumably homogenous Bentheim sandstone sample affected the overall sweep efficiency and preferred flow path of the injected brine. Local displacement was derived from independent PET and MR signals, with an excellent correspondence on the core and sub-core scale. A low-porous region, identified by both PET and MR, caused deviations from ideal displacement behavior.

4. Conclusion

Synergy of a new multimodal imaging method was demonstrated in core scale water resources research for the first time. Multimodal PET-MR imaging represents an opportunity to image and quantify up to three fluid phases in opaque systems within the same field of view and time frame. Local saturation values were derived from independent PET and MR signals, with an excellent correspondence on the core and sub-core scale. The unambiguous correlation of phase identification across modality and injection schemes enables us to conclude that PET-MR represents a scientific advancement with potentially high future impact in geoscientific research.

Declaration of Competing Interest

The authors declare no conflicts of interests.

Acknowledgements

Supplementary materials

References

Boutchko, R., Rayz, V.L., Vandehey, N.T., O'Neil, J.P., Budinger, T.F., Nico, P.S., Druhan, J.L., Saloner, D.A., Gullberg, G.T., Moses, W.W., 2012. Imaging and modeling of flow in porous media using clinical nuclear emission tomography systems and computational fluid dynamics. J. Appl. Geophys. 76, 74–81.

Brattekås, B., Eide, Ø., Johansen, S.A., Vasshus, S.S., Polden, A.G., Fernø, M.A., 2019. Foam and mobility control in natural fracture networks. Transp. Porous Media 131, 157–174.

Brattekås, B., Haugen, M., 2020. Explicit tracking of CO_2-flow at the core scale using micro-positron emission tomography (µPET). J. Nat. Gas Sci. Eng. 77.

Brattekås, B., Steinsbø, M., Graue, A., Fernø, M.A., Espedal, H., Seright, R.S., 2017. New insight into wormhole formation in polymer gel during water chase floods with positron emission tomography. SPE J. 22 (01), 32–40.

Dechsiri, C., Ghione, A., van de Wiel, F., Dehling, H.G., Paans, A.M.J., Hoffmann, A.C., 2005. Positron emission tomography applied to fluidization engineering. Can. J. Chem. Eng. 83 (1), 88–96.

Degueldre, C., Pleinert, H., Maguire, P., Lehman, E., Missimer, J., Hammer, J., Leenders, K., Böck, H., Townsend, D., 1996. Porosity and pathway determination in crystalline rock by positron emission tomography and neutron radiography. Earth Planet. Sci. Lett. 140 (1–4), 213–225.

Ersland, G., Fernø, M.A., Graue, A., Baldwin, B.A., Stevens, J., 2010a. Complementary imaging of oil recovery mechanisms in fractured reservoirs. Chem. Eng. J. 158, 32–38.

Ersland, G., Husebø, J., Graue, A., Baldwin, B.A., Howard, J.J., Stevens, J.C., 2010b. Measuring gas hydrate formation and exchange with CO_2 in Bentheim sandstone using MRI tomography. Chem. Eng. J. 158, 32–38.

Fernø, M.A., Gauteplass, J., Hauge, L.P., Abell, G.E., Adamsen, T.C.H., Graue, A., 2015a. Combined positron emission tomography and computed tomography to visualize and quantify fluid flow in sedimentary rocks. Water Resour. Res. 51 (9), 7811–7819.

Fernø, M.A., Hauge, L.P., Rognmo, A.U., Gauteplass, J., Graue, A., 2015b. Flow visualization of CO_2 in tight shale formations at reservoir conditions. Geophys. Res. Lett. 42, 7414–7419.

Føyen, T., Fernø, M.A., Brattekås, B., 2019. The Effects of nonuniform wettability and heterogeneity on induction time and onset of spontaneous imbibition. SPE J. 24 (3), 1192–1200.

Haugan, A., 2000. A low-cost PET system for use in flow experiments of porous media. SPE Annual Technical Conference and Exhibition Dallas, TX.

Heindel, T.J., 2011. A review of X-ray flow visualization with applications to multiphase flows. J. Fluid Eng.-T ASME 133 (7).

Hoff, W.D., Wilson, M.A., Benton, D.M., Hawkesworth, M.R., Parker, D.J., Fowles, P., 1996. The use of positron emission tomography to monitor unsaturated water flow within porous construction materials. J. Mater. Sci. Lett. 15 (13), 1101–1104.

Howard, J.J., 1998. Quantitative estimates of porous media wettability from proton NMR measurements. Magn. Reson. Imaging 5, 529–533.

Keereman, V., Mollet, P., Berker, Y., Schulz, V., Vandenberghe, S., 2013. Challenges and current methods for attenuation correction in PET/MR. Magn. Reson. Mater. Phys. Biol. Med. 26 (1), 81–98.

Khalili, A., Basu, A.J., Pietrzyk, U., 1998. Flow visualization in porous media via positron emission tomography. Phys. Fluids 10 (4), 1031–1033.

Krevor, S.C.M., Pini, R., Li, B., Benson, S.M., 2011. Capillary heterogeneity trapping of CO_2 in a sandstone rock at reservoir conditions. Geophys. Res. Lett. 38 (15), L15401.

Kulenkampff, J., Gruundig, M., Richter, M., Enzmann, F., 2008. Evaluation of positron-emission-tomography for visualisation of migration processes in geomaterials. Phys. Chem. Earth 33 (14-16), 937–942.

Maguire, R.P., Missimer, J.H., Emert, F., Townsend, D.W., Dollinger, H., Leenders, K.L., 1997. Positron emission tomography of large rock samples using a multiring PET instrument. IEEE T Nucl. Sci. 44 (1), 26–30.

Mitchell, J., Chandrasekera, T.C., Holland, D.J., Gladden, L.F., Fordham, E.J., 2013. "Magnetic resonance imaging in laboratory petrophysical core analysis. Phys. Rep. 526 (3), 165–225. https://doi.org/10.1016/j.physrep.2013.01.003.

Ogilvie, S.R., Orribo, J.M., Glover, P.W.J., 2001. The influence of deformation bands upon fluid flow using profile permeametry and positron emission tomography. Geophys. Res. Lett. 28 (1), 61–64.

Pini, R., Vandehey, N.T., Druhan, J., O'Neil, J.P., Benson, S.M., 2016. Quantifying solute spreading and mixing in reservoir rocks using 3-D PET imaging. J. Fluid Mech. 796, 558–589.

Vasco, D.W., Pride, S.R., Zahasky, C., Benson, S.M., 2018. Calcuating trajectories associated with solute transport in a heterogeneous medium. Water Resour. Res. 54 (9), 6890–6908.

Werth, C.J., Zhang, C., Brusseau, M.L., Oostrom, M., Baumann, T., 2010. "A review of non-invasive imaging methods and applications in contaminant hydrogeology research. J. Contam. Hydrol. 113, 1–4.

Zahasky, C., Benson, S.M., 2018. Micro-positron emission tomography for measuring sub-core scale single and multiphase transport parameters in porous media. Adv. Water Res. 115, 1–16.

Zahasky, C., Kurotori, T., Pini, R., Benson, S.M., 2019. Positron emission tomography in water resources and subsurface energy resources engineering research. Adv. Water Res. 127, 39–52 May 2019.